



Cite this: *Chem. Commun.*, 2019, 55, 14182

Received 18th September 2019,
Accepted 27th October 2019

DOI: 10.1039/c9cc07322a

rsc.li/chemcomm

A lysosome-specific near-infrared fluorescent probe for *in vitro* cancer cell detection and non-invasive *in vivo* imaging†

Rakesh Mengji,^a Chiranjit Acharya,^a Venugopal Vangala^{ab} and Avijit Jana^{*,abc}

Near-infrared (NIR) fluorescent probes have been developed as potential bio-materials having profound applications in diagnosis and clinical practice. Herein, we wish to disclose a highly photo-stable ultra-bright NIR probe for the specific detection of lysosomes in numerous cell lines. Furthermore, the applicability of the developed NIR probe was evaluated for *in vivo* imaging.

The fluorescence imaging technique to visualize living cell processes or even a whole organism in real-time has been revealed to be the central research interest in recent years.^{1–3} However, the major shortcomings of the fluorescence imaging technique are low tissue penetration depth, nonspecific background fluorescence and inadequate photostability of the fluorophore. Among various fluorescence imaging techniques, near-infrared (NIR) fluorescence imaging has been found to be prudent due to its excellent deep-tissue penetration potential and deep-tissue imaging without any invasion.⁴ Therefore, a NIR fluorophore with a high specificity to a specific bio-analyte is highly desirable to visualize the real time dynamics of an associated disease.^{5,6} Recently, several NIR probes have been reported for various applications, including cancer diagnosis.^{1,7–9} However, the accurate detection of cancer analytes still remains challenging owing to the lack of suitably functionalized NIR probes. In recent years, the epidemiology of cancer has been found to be one of the major causes of reduced mortality index.¹⁰ Prudent cancer therapy involves early detection followed by parallel treatment of cancer.^{10,11} However, it needs suitable diagnostic development, which is a demanding task in modern cancer research.¹¹ The advancement of science and technology has offered many sophisticated imaging techniques, including magnetic resonance imaging (MRI), positron emission tomography

(PET), X-ray radiography, computed tomography (CT) and ultrasound imaging as diagnostic tools for cancer detection. In spite of the certain advantages of these techniques, which include user-friendliness, easy availability and long-range tissue penetration, they suffered from foremost limitations, which include lack of selectivity and sensitivity, inadequate efficiency for envisioning real-time dynamics and radiation hazards.^{12–14} Therefore, it is worth demanding to develop a quantized technique having limited or no cellular invasion with high selectivity and sensitivity along with excellent resolution modality for the detection of cancer.¹³ As a result, NIR fluorescent imaging has been introduced as an emerging imperative for the detection of cancer at an early stage.^{6,14} Hence, there is an urgent need for the development of highly stable NIR fluorophores with high specificity to cancer analytes for analytical and clinical optical imaging.⁹

Several NIR fluorescent imaging probes comprising both organic and inorganic fluorophores have been illustrated in literature in recent times. Inorganic NIR probes, including quantum dots and other inorganic nanoparticles (NPs), were found to be expensive with considerable cytotoxicity, which triggered a switch in research focus to the search for suitable organic NIR probes.^{15–20}

Among a number of organic NIR fluorescent probes, perylene derivatives have attained considerable interest since they meet the criteria for good NIR probes, which include red to NIR excitation, high fluorescence quantum yields, high absorption coefficients, large Stokes shifts, high stability in biological systems, exceptional stability against photo-bleaching and synthetic simplicity.^{6,21–23} With this idea, several attempts have been made to synthesize a perylene-based fluorophore, but only a few have been actualized for *in vivo* deep tissue bio-imaging.^{5,6,21–23} Herein, we wish to disclose a perylene monoimide (PeIm)-based new NIR fluorescent probe, which could selectively and non-invasively detect and sense cancer cells over noncancerous cells *in vitro* and could also be a practical tool for *in vivo* NIR imaging, as schematically shown in Scheme 1.

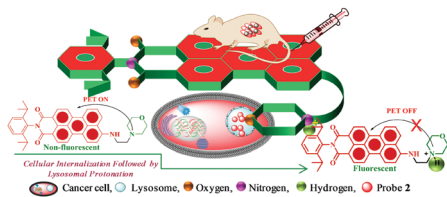
To synthesize the perylene monoimide-based NIR probe, we started with commercially-available perylene-3,4,9,10-tetracarboxylic dianhydride, which was converted to *N*-(2,6-di-isopropylphenyl)-9-bromoperylene-3,4-dicarboximide (**1**) following a literature

^a Department of Applied Biology, CSIR-Indian Institute of Chemical Technology, Hyderabad 500007, India

^b Academy of Scientific and Innovative Research (AcSIR), Ghaziabad 201002, India

^c Department of Organic Synthesis and Process Chemistry, CSIR-Indian Institute of Chemical Technology, Hyderabad 500007, India. E-mail: janaavijit2@gmail.com, Avijit@iict.res.in

† Electronic supplementary information (ESI) available. See DOI: 10.1039/c9cc07322a



Scheme 1 Schematic of the perylene monoimide (PeIm)-based NIR probe for *in vitro* and *in vivo* bio-imaging.

procedure.²⁴ Finally, **1** was coupled with 2-morpholinoethan-1-amine to obtain the final NIR probe, *N*-(2,6-di-isopropylphenyl)-9-(2-morpholinoethan-1-amine)perylene-3,4-dicarboximide (**2**) as shown in Scheme S1 (ESI[†]).

After successful synthesis and characterization, the photophysical properties of probe **2** were investigated in detail in different solvent systems. The absorption spectra of probe **2** in an acetonitrile solution (1×10^{-5} M) revealed an intense absorption band centered at 610 nm, while the emission maxima was red-shifted at about 700 nm (Fig. 1a). When the emission spectra of **2** were recorded in different solvents, a gradual bathochromic shift with increased emission intensity on increasing the solvent polarity was observed (Fig. 1b). This can be attributed to the suppression of the photoinduced electron transfer (PET) from the morpholine N-atom to the PeIm chromophore. In order to understand the effect of H-bonding on the emission properties of the probe **2**, emission spectra were recorded in ACN/water binary mixtures. It was noted that an increase in the percentage of water resulted in a further bathochromic shift in the emission maxima to around 725 nm. However, a gradual decrease in the emission intensity of the probe **2** (Fig. 1c) was observed because of the formation of aggregates. On the other hand, when the emission spectra of **2** were recorded at a different pH, it was observed that the probe **2** was less emissive in neutral or in basic pH. However, on lowering the solution pH (6.0–3.0), the emission intensity was greatly enhanced (Fig. 1d), which suggested the protonation of the morpholine N-atom and thereby the dissolution of the aggregates and also the complete suppression of the PET process as mentioned earlier.

It has been well documented that a dysregulated pH is an adaptive feature for most of the cancers irrespective of their tissue

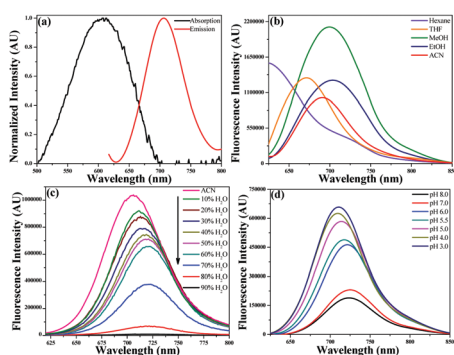


Fig. 1 (a) Normalized absorption and emission spectra of **2** in ACN. Emission spectra of **2** in (b) different solvents, (c) a binary mixture of ACN and water and (d) in a different pH.

origin or genetic background.¹⁰ The tumor microenvironment is mildly acidic due to the distorted metabolism, which is also known as the “Warburg effect” of tumors and relative hypoxia.²⁵ The strong emission of the probe **2** in the pH range of 3.0–6.0, which actually covers both normal and abnormal lysosomal pH, indicated that the probe **2** can be an ideal candidate in the systematic mapping of the cellular pH and thereby can be able to distinguish cancerous cells over noncancerous cells.

Since the photophysical properties of the probe **2** revealed its strong absorption and emission in the NIR region and high sensitivity towards the solvent pH, it was employed for *in vitro* imaging studies on the cancerous MCF7 cell line to understand its potential in cell imaging (Fig. S2–S4, ESI[†]). In order to understand the cytoplasmic distribution of **2** in detail, cells were counterstained separately with commercially available lysotracker green (LTG) and mitotracker green (MTG), followed by recording images using a confocal laser scanning microscope (CLSM). The counterstaining experiment clearly revealed the co-localization of **2** (yellow fluorescence in Fig. 2(i)d) with LTG (Fig. 2(i)a–d and Fig. S5, S6, ESI[†]), but not with MTG (Fig. 2(ii)a–d and Fig. S7, S8, ESI[†]). These observations clearly signify that the probe **2** is exclusively localized in the lysosomes of the MCF7 cell line. Furthermore, to clarify whether the lysosomal localization of the probe **2** was its exclusive property, similar subcellular localization experiments with **2** were performed on a noncancerous CHO cell line following a similar protocol to that used for the MCF7 cell line. As expected, the probe **2** was internalized by the CHO cells (Fig. S9 and S10, ESI[†]) and profoundly distributed in the lysosome (Fig. 2(iii)a–d, yellow fluorescence in Fig. 2(iii)d and Fig. S11, S12, ESI[†]), but not in the mitochondria (Fig. 2(iv)a–d and Fig. S13, S14, ESI[†]). Furthermore, the quantitative colocalization studies conducted by means of scatter plot and colocalization pixel map analysis clearly demonstrate a profound localization of probe **2** in the lysosome (Fig. 2(i)e and (iii)e) over mitochondria (Fig. 2(ii)e and (iv)e). Although, the subcellular distribution of the probe **2** in both

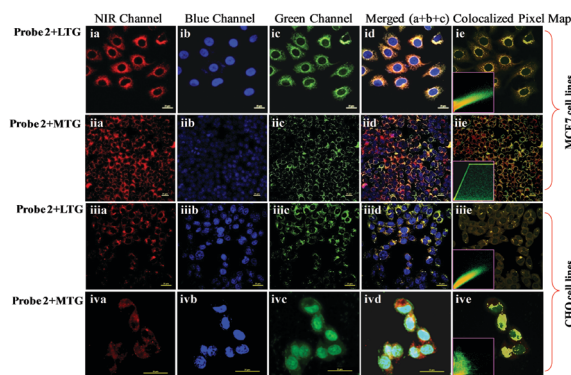


Fig. 2 CLSM images of the MCF7 cell lines incubated with **2**, DAPI, LTG and MTG: (a) NIR channel, (b) blue channel, (c) green channel, (d) merged images and (e) a colocalization pixel map of the corresponding NIR and green channel. Insets of (ie–ive) are the corresponding scatter plots. (ie and iie) Concentrated pixels along the diagonals indicate a high degree of colocalization of probe **2** and LTG; (iie and ive) scattered pixels along the diagonals indicate a lower degree of colocalization of probe **2** and MTG. Scale bar: 25 μ m.

cancerous MCF7 cells and noncancerous CHO cells revealed a profound accumulation in the acidic lysosomal compartment, the most interesting observation was the emission signal from the MCF7 cells (Fig. 2(i)a–d), which was remarkably high with respect to the signal from the CHO cells (Fig. 2(iii)a–d). For the better visualization of the pH-dependent colorimetric differences between the cancerous MCF7 cells and noncancerous CHO cells, 3D Z-stack images with higher magnification are displayed in Fig. 3, which clearly show a higher fluorescence intensity in the MCF7 cells compared to the CHO cells. Furthermore, the degree of cellular uptake of **2** and thereby colorimetric differences *in vitro* were also assessed quantitatively by means of flow cytometry using both MCF 7 (Fig. 3c) and CHO (Fig. 3d) cell lines. Significantly higher degrees of cellular uptake were observed over time only for the cancerous MCF7 cells (Fig. 3c). This remarkably high emission intensity in the MCF7 cells (Fig. 3a and c) can be correlated to the inherent acidic nature of the cancerous cells over the normal CHO cells (Fig. 3b and d). Therefore, the probe **2** can be an ideal diagnostic tool for the discrimination of cancerous and noncancerous cells *in vitro*.

Now, the lysosome exclusive localization of the probe **2** could be attributed to either the exclusive physical localization of **2** in the lysosomes or its presence in other organelles in the endocytic pathway, but it was only emissive in the lysosome due to the protonation of the morpholine N-atom at lower pH, whereas in other organelles, it remained fluorescence silent.

To understand the 2nd postulate, *i.e.* the probe **2** may be located in other organelles but was in the fluorescence OFF state, MCF7 cells were first incubated with **2** in media at pH 7.4 for 4 h; followed this, the cells were fixed and imaged using CLMS (Fig. 4(i)a–e). Then, the medium was discarded and fresh medium of pH 4.5 (pH was adjusted using HCl) was added, and the cells were further imaged with the same microscopic parameters after 20 min. The results revealed a significantly increased fluorescence within the cells (Fig. 4(ii)a–e and Fig. S17, S18, ESI[†]). The increased fluorescence intensity at lower pH was because it forced the probe **2** to be protonated within the organelles of a naturally higher pH environment. This clearly shows that probe **2**, which was located in the lysosomes, was only in the fluorescent ON state under normal cellular conditions.

To explore the potential of the probe **2** in cancer diagnosis *in vitro*, controlled imaging experiments were performed on a set of four different cancer cell lines, namely, RKO (Fig. 5(i)a–e), U87 (Fig. 5(ii)a–e), CT26 (Fig. 5(iii)a–e), and GL261 (Fig. 5(iv)a–e) as well as the normal Human embryonic kidney 293 (HEK 293)

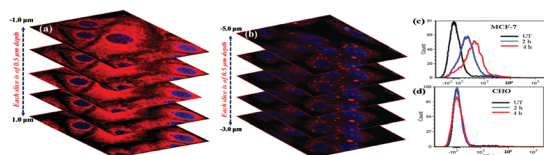


Fig. 3 CLSM images and flow cytometry data of the MCF7 and CHO cell lines incubated with probe **2** and DAPI: (a) MCF7 and (b) CHO (all 3D Z stack images). (c and d) Corresponding flow cytometry data in different time intervals for the MCF7 and CHO cells, respectively.

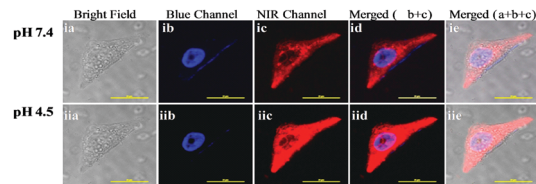


Fig. 4 CLSM images of MCF7 cells incubated with **2** and DAPI (ia–e) at pH 7.4. (iia–e) The same cell imaged after the buffer was changed to pH 4.5 with all the same microscopic parameters. Scale bar: 25 μ m.

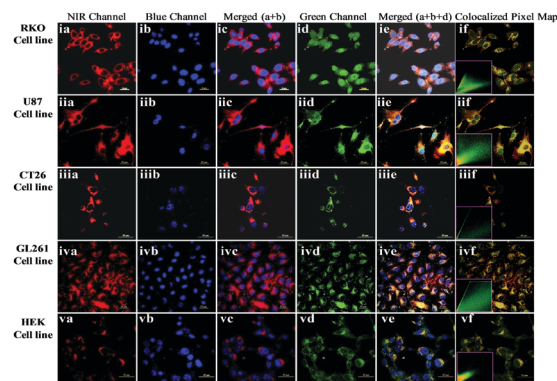


Fig. 5 CLSM images of (i) RKO, (ii) U87, (iii) CT26, (iv) GL261 and (v) HEK 293 cell lines incubated with probe **2**, DAPI and LTG: (a) NIR, (b) blue channel, (c) merged image of (a and b), (d) green channel, (e) merged images (a, b and d, and f) colocalization pixel map of the corresponding NIR and green channel. Inset in (if–vf) is the corresponding scatter plot: concentrated pixels along the diagonals indicate high degree of colocalization of probe **2** and LTG. Scale bar: 25 μ m.

(Fig. 5(v)a–e) cell line. The controlled imaging experiment clearly shows a profound emission intensity for all the four cancerous cell lines (Fig. 5(i–iv)a–e) in comparison to the normal HEK 293 cell line (Fig. 5(v)a–e).

We also tested the possibility of live cell imaging using the probe **2** to establish it as a readily available bioanalytical probe for both *in vitro* and *in vivo* applications. MCF7 cells were pretreated with **2** and LTG for 4 h. Cells were incubated at 37 $^{\circ}$ C under 5% CO₂ and imaged at time points from 0 to 30 min using confocal microscopy. In the CLSM images (Fig. S15(i)a–e, ESI[†]), lysosomes can be clearly seen as point-like fluorescent vesicles in the periphery of the cell nucleus.

Images were taken continuously at 15 min intervals to track the fluorescent lysosomes over time, which showed the gradual movement of the lysosomes towards the edge of the cell (Fig. S15(i)b–(iii)b, ESI[†]), marked in the circle). It was also observed that the number of fluorescent vesicles decreased over time with the appearance of bigger and brighter vesicles, suggesting the fusion of several lysosomes²⁶ over the course of cellular events. Therefore, the probe **2** was readily internalized by the living MCF7 cells, which allowed us to visualize its real-time dynamics, which further confirmed the applicability of probe **2** as an efficient diagnostic tool for the evaluation of lysosomal health.

The advantages of a NIR fluorophore for *in vivo* imaging due to the transparency of the tissues in the NIR window were previously described. To test the *in vivo* imaging performance of

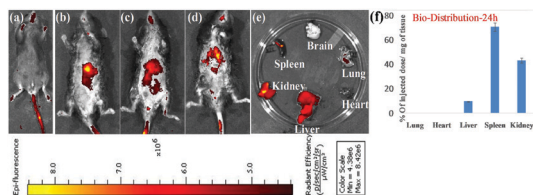


Fig. 6 *In vivo* NIR imaging of **2** in female C57BL/6J mice: (a) after 0 h, (b) 8 h, (c) 16 h, and (d) 24 h of i.v. of **2**. (e) *Ex vivo* images of different organs after 24 h. (f) % distribution of probe **2** in per unit mass of the respective organs.

2, an intravenous (i.v.) tail vein injection of **2** (4 mg kg^{-1}) was administered to 6–8 weeks old female C57BL/6J mice. Following this, images were acquired at regular intervals over the course of 24 h (Fig. 6a–d).

To have a better understanding of the biodistribution profile of **2**, mice were sacrificed after 24 h and different organs were isolated and *ex vivo* imaged. The representative *ex vivo* images showed the highest emission in the liver, followed by the kidney and spleen (Fig. 6e), suggesting the gradual clearance of the probe **2** from the body through urine over time. The probe **2** was extracted in acidic isopropanol from different organs at 24 h post i.v., and the biodistribution of **2** per unit mass of the corresponding organs was determined. The results showed that a major distribution of the administered probe **2** was observed in the spleen ($>60\%$), followed by the kidney ($>30\%$) and liver ($<10\%$) (Fig. 6f).

In order to validate the probe **2** to be applicable for practical imaging, its *in vivo* toxicity was investigated on the C57BL/6J mouse model. C57BL/6J mice (4–6 weeks old) were treated with **2** at two different concentrations (4 and 16 mg kg^{-1}). In addition, in a control experiment, the mice were treated with Hanks' balanced salt solution (HBSS) by i.v. injection every alternative day for a period of 4 weeks. The weight and movement of all the mice were checked daily. During the entire treatment (4 weeks) with the probe **2**, the body weight and movement of the mice were found to be similar for all of the treated mice (data not shown) as well as the mice used for the control experiment, which clearly shows that the corresponding doses of **2** were in a tolerable limit for all of the mice. After the completion of the treatment, mice were sacrificed and the tissues of five major organs, *i.e.*, heart, kidney, liver, lung, and spleen, were collected and subjected to hematoxylin and eosin (HE) staining, which showed no visible tissue necrosis for all five major organs (Fig. S16, ESI†). Thus, the *in vivo* toxicology studies clearly demonstrate that the probe **2** could be considered safe for future applications.

In conclusion, we developed a perylene-derived highly photostable ultra-bright NIR probe, which is highly specific for lysosome imaging in both fixed and live cells, and exploited to discriminate cancer cells over the normal cells *in vitro*. It was

also employed to visualize the real-time dynamics of lysosomal movement in live MCF7 cells. Furthermore, it was successfully used for *in vivo* deep-tissue imaging of a C57BL/6J mice model. The present system could be a promising candidate for further bioanalytical, diagnostic and image-guided therapeutic development.

AJ and RM thank DST for the INSPIRE Faculty Grant (IFA15, CH171, GAP0546), CA thanks SERB for the NPDF grant and VV thanks CSIR for the fellowship. The CSIR-IICT Communication number for this manuscript is IICT/Pubs./2019/317.

Conflicts of interest

There are no conflicts to declare.

Notes and references

- D. Cheng, J. Peng, Y. Lv, D. Su, D. Liu, M. Chen, L. Yuan and X. Zhang, *J. Am. Chem. Soc.*, 2019, **141**, 6352.
- D. Cheng, Y. Pan, L. Wang, Z. Zeng, L. Yuan, X. Zhang and Y. T. Chang, *J. Am. Chem. Soc.*, 2017, **139**, 285.
- Q. Gong, W. Shi, L. Li and H. Ma, *Chem. Sci.*, 2016, **7**, 788.
- S. Luo, E. Zhang, Y. Su, T. Cheng and C. Shi, *Biomaterials*, 2011, **32**, 7127.
- A. Jana, L. Bai, X. Li, H. Ågren and Y. Zhao, *ACS Appl. Mater. Interfaces*, 2016, **8**, 2336.
- R. Wang and F. Zhang, *J. Mater. Chem. B*, 2014, **2**, 2422.
- J. Fan, H. Dong, M. Hu, J. Wang, H. Zhang, H. Zhu, W. Sun and X. Peng, *Chem. Commun.*, 2014, **50**, 882.
- P. Wang, Y. Fan, L. Lu, L. Liu, L. Fan, M. Zhao, Y. Xie, C. Xu and F. Zhang, *Nat. Commun.*, 2018, **9**, 2898.
- C.-H. Tung, J. Qi, L. Hu, M. S. Han and Y. Kim, *Theranostics*, 2015, **5**, 1166.
- F. Bray, J. Ferlay, I. Soerjomataram, R. L. Siegel, L. A. Torre and A. Jemal, *Ca-Cancer J. Clin.*, 2018, **68**, 394.
- R. T. Greenlee, T. Murray, S. Bolden and P. A. Wingo, *Ca-Cancer J. Clin.*, 2000, **50**, 7.
- Y. Kitagawa, S. Nishizawa, K. Sano, T. Ogasawara, M. Nakamura, N. Sadato, M. Yoshida and Y. Yonekura, *J. Nucl. Med.*, 2003, **44**, 198.
- L. Fass, *Mol. Oncol.*, 2008, **2**, 115.
- A. Yuan, J. Wu, X. Tang, L. Zhao, F. Xu and Y. Hu, *J. Pharm. Sci.*, 2013, **102**, 6.
- A. Nel, T. Xia, L. Mädler and N. Li, *Science*, 2006, **311**, 622.
- M. N. Moore, *Environ. Int.*, 2006, **32**, 967.
- M. C. Mancini, B. A. Kairdolf, A. M. Smith and S. Nie, *J. Am. Chem. Soc.*, 2008, **130**, 10836.
- A. Hoshino, S. Hanada and K. Yamamoto, *Arch. Toxicol.*, 2011, **85**, 707.
- A. M. Alkilany, P. K. Nagaria, C. R. Hexel, T. J. Shaw, C. J. Murphy and M. D. Wyatt, *Small*, 2009, **5**(6), 701.
- A. Jana, K. S. P. Devi, T. K. Maiti and N. D. P. Singh, *J. Am. Chem. Soc.*, 2012, **134**, 7656.
- A. Jana, K. T. Nguyen, X. Li, P. Zhu, N. S. Tan, H. Ågren and Y. Zhao, *ACS Nano*, 2014, **8**, 5939.
- H. Iwashita, S. Torii, N. Nagahora, M. Ishiyama, K. Shioji, K. Sasamoto, S. Shimizu and K. Okuma, *ACS Chem. Biol.*, 2017, **12**, 2546.
- C.-K. Tsung, X. Kou, Q. Shi, J. Zhang, M. H. Yeung, J. Wang and G. D. Stucky, *J. Am. Chem. Soc.*, 2006, **128**, 5352.
- K. M. Lefler, D. T. Co and M. R. Wasielewski, *J. Phys. Chem. Lett.*, 2012, **3**, 3798.
- V. Estrella, T. Chen, M. Lloyd, J. Wojtkowiak, H. H. Cornnell, A. I. Hashim, K. Bailey, Y. Balagurunathan, J. M. Rothberg, B. F. Sloane, J. Johnson, R. A. Gatenby and R. Gillies, *J. Cancer Res.*, 2013, **73**, 1524.
- Q. Ba, G. Raghavan, K. Kiselyov and G. Yang, *Cell Rep.*, 2018, **23**, 3591.